Influence of multi-transverse crack on cantilever shaft

**Jajneswar Nanda, LD Das, Sandeep Das and
Harish Chandra Das**

Abstract

Analysis of transversely loaded cantilever shaft having multiple cracks is investigated in this paper. The behavior of cracks locations and sizes on vibration parameters is presented taking the advantage of reduction in stiffness of shaft from fracture mechanics. The shaft is subjected to static axial and bending load for given angle of twist along its longitudinal direction. Using the principle strain energy release rate and stress intensity factor (for plain stress and strain condition), the natural frequencies with their mode shapes at different crack locations with its depths are evaluated. The result obtained from theoretical method has been verified with the advantage of adaptive neuro-fuzzy inference system (ANFIS) using the modal parameter of cracked shaft. The vibration parameters such as first three non-dimensional natural frequencies with their mode shapes at different locations and depths are supplied to ANFIS to optimize the results. The crack location and size predicted from ANFIS model are verified with the theoretical data with acceptable error. The surface plot, residual error, and probability plot obtained from ANFIS are showing the effectiveness of theoretical method. Research work has been extended to set up an experimental model to strengthen both theoretical and ANFIS work. The paper basically focused on error percentage obtained from the theoretical result with ANFIS and experimental work. It is found that the error percentage in ANFIS and experimental analysis are ±2% and ±7.33% respectively with respect to theoretical analysis. The present method is simple and can be easily extended to complex structure with different orientation of multiple cracks for any structural analysis.

Keywords

Vibration, multiple cracks, shaft, natural frequency, mode shape, adaptive neuro-fuzzy inference system, experimental analysis

Introduction

The basis of linear elastic fracture mechanics (LEFM) is to study the behavior of crack in machine component like shaft, beam, or plate. Initiation of crack in any structure is not important. However, the growth rate of crack leads to catastrophic failure of machine component. The physical

Department of Mechanical Engineering, Siksha 'O' Anusandhan University, Bhubaneswar, India

Corresponding author:
Jajneswar Nanda, Department of Mechanical Engineering, Siksha 'O' Anusandhan University, Bhubaneswar 751003, Odisha, India.
Email: nandajajneswar@yahoo.in

characteristics of a structure due to crack alter its dynamic response. Therefore, early detection of crack is desirable in modern machinery to avoid catastrophic failures of machines' component. Diagnosis of fault before and after the damage has been a challenging task for the researcher in the last few decades across the globe. Various nondestructive techniques and health monitoring system came forward to solve nonlinear problem with less cost and better accuracy. Stress intensity factor (SIF) is the key parameter that deals with growth rate of crack and it depends on the applied loading and geometry of structure. The rate at which strain energy released depends on SIF, which is a function of location of crack with depth. Apart from conventional methods, nondestructive techniques (NDT) and AI technique can be applied actively to detect the faults in all dynamic structures within a short span of time. The key parameters for vibration analysis are depth of crack with its location.

Shooshtari and Khajavi (2010) studied the vibration characteristic of tapered beam with its abrupt jumps in crack section using strain-interpolating functions. They determined the exact stiffness matrix and interpolating function using principle of virtual work. Noble works were presented by Dixit and Hanagud (2011) to determine mode shapes and natural frequencies through perturbation method. The damage indexes such as stiffness and mass per unit length are independent of beam properties presented by Liu et al. (2011). They used an edge-based smooth finite element method for simulating singular stress field for mode-1 fracture. Moore et al. (2011) implemented Byes theorem, taking Markov-chain Monte Carlo implementation for determining crack parameters and their probability distribution. Palmeri and Cicirello (2011) formulated a model for slender Euler–Bernoulli beam and short Timoshenko beam having multiple cracks with various crack depths. Rezaee and Hassannejad (2011) adopted crack as fatigue and change in the local stiffness as a nonlinear-dependent function. The dynamic response of the cracked beam has been calculated using mechanical energy balance model. Rubio et al. (2011) represented the flexibility matrix through the polynomial fitting of the SIFs, by integrating elliptical front and compared the results obtained through finite element method. Abortive change in strength due to hole in laminated composite glass-epoxy fiber was given by Sen et al. (2011) under various orientation of fiber at different loading. Experiments were conducted to investigate the failure analysis under various material and geometrical parameters. They concluded that bearing strength and failure mode tenaciously modified due to presence of hole or bolt joints. Lundmark and Varna (2011) formulated an interaction function to measure the crack opening displacement. Interaction function has been formulated by the using the results of finite elements morphology. Ignoring the geometrical and material properties of cross-ply laminate,the interaction function represented as a crack density to foretell the reduction in stiffness at the crack layar. Zhu et al. articulated a model to compute fatigue life at low amplitude using Miner's rule. Different fuzzy set rule has been employed to improve the Miner rule. The outcome derived from the model is supported with experimental results. A new approach was made by Pham et al. (2012) for developing a model intimating material property degradation method (MPDM) and cohesive element (CE) for radical failure of carbon-epoxy composite. Various theories of failure has been introduced to study the degradation of material properties. It is concluded that the reduction in strength due to notch increases on increasing the specimen size. The expected results were compared with the experimental data and good agreement was found. Movaghghar and Lvov (2012) recommended a model made up of composite material used for wind turbine blade. The specific blade model is intended for maximum elastic strain energy achived at the growth rate of damage for different critical load position using ANSYS. Critical stresses and fatigue life were computed at resonance condition. Nanda and Das (2013) analyzed fault in a cracked structure using genetic algorithm (GA) technique. They presented a crack cantilever beam to determine the natural frequency through numerical method and validated results by

using GA. A new hybrid model was presented by Nanda et al. (2013) taking multiple adaptive neuro-fuzzy interface system (MANFIS) for crack diagnosis in the fixed shaft using changes in vibration parameter. Saeed et al. (2012) presented a crack diagnosis in the curvilinear beam using frequency functions and artificial neural network (ANN) and showed results with good agreement. Sayyad et al. (2013) provided a proper procedure to verify the intensity of crack with its location regulating the data of axial vibration for different beam structure. The effectiveness of two first natural frequencies for determination of crack parameters is employed theoretically. The results of theoretical analysis is validated by experimental approach and suitable agreement was found.

The flexural vibration in cantilever beam having various transverse crack with its location and size has been detected. Suresh et al. (2004) analytically used modal parameters and modelled the crack as rotational spring. The results obtained from the modal analysis have been optimized by neural network and Newton–Raphson method. GA is a multi-objective optimizing technique, which wasused by Cheng and Tham (2003) for multi-output with multi-input parameter. The input parameter used for GA are relative to all the three natural frequencies with their mode shape, crack location, and size trained up to the GA controller. The output of GA is the crack location and depth, which is verified with the experimental data. Chandrashekhar and Ganguli (2009) have expounded a fuzzy logic system for detection of crack. They evaluated the relation between changes in the modal frequency with change in material properties which helped them in developing a robust fuzzy model for detection of crack parameters. Studies presented by Panigrahi et al. (2009) consisted of an objective function for verifying microscopic fatigue crack in a uniform strength beam using a residual force method and GA. They investigated the crack parameters by varying both width and depth but keeping the uniform strength as constant. Zachanias et al. (2004) focused on detecting damage on crates of beverages using ANN for locating crack position and size in various structural designs. The input data to ANN provided by frequency responses spectra was obtained by finite element, theoretical, and experimental method and a good agreement was found with the existing data.

Theoretical analysis of shaft

With the help of linear fracture mechanics theory and taking the strain energy release rate and stress intensity factor, the mode shapes, natural frequencies, and stiffness of the steel cracked cantilever shaft have been calculated as follows.

Estimation of local flexibility of damaged shaft under axial and bending load

A multi-cracked cantilever shaft of diameter D is represented in Figure 1. Two transverse surface cracks are presented at two locations L_1 and L_2 with depth b_1 and b_2 from the fixed end (Figure 3).
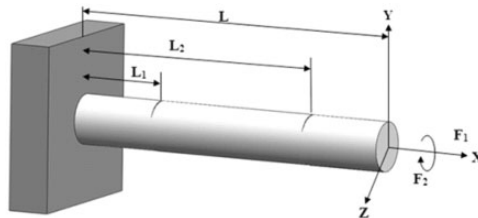
Figure 1. Shaft with multiple cracks.
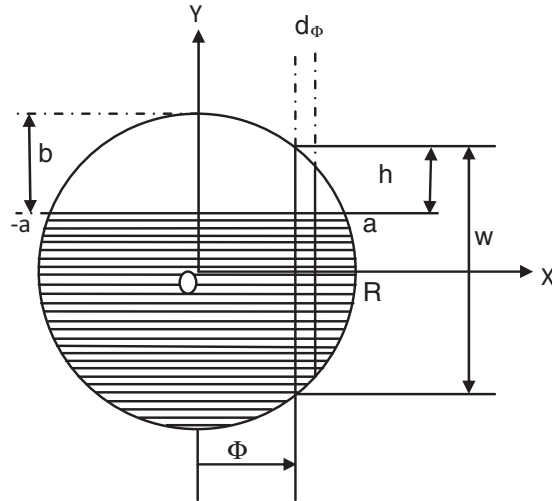
Figure 2. Geometry of cracked surface.
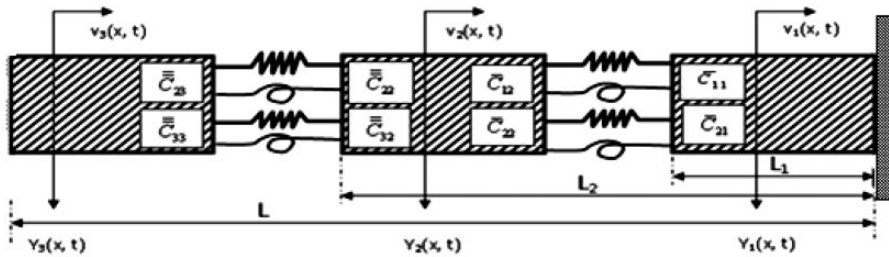
Figure 3. Crack model.

Both the cracks result in a coupling effect yielding both longitudinal and transverse motion of the shaft. An axial force F_1 and bending force F_2 are applied at free end of the shaft. Due to the presence of cracks, a local flexibility will be interposed with the order of 2×2 matrix. The geometry of cracked surface is shown in Figure 2.

The rate of strain energy released during fracture is J_e where

$$J_e = \frac{1}{E'}(C_{11} + C_{12})^2 \tag{1}$$

For plane strain condition, $\quad \dfrac{1}{E'} = \dfrac{1 - v^2}{E}$

For plane stress condition, $\quad \dfrac{1}{E'} = \dfrac{1}{E}$

here, γ is the Poisson's ratio and E is the Young's modulus of elasticity. C_{11} and C_{12} represents stress intensity factors of first mode for given load F_1 and F_2, respectively. The values of local stiffness

factor from fracture mechanics can be calculated by taking the rectangular strip d_Φ as given in Figure 2.

$$\text{Height of the element} \quad w = 2\sqrt{(R^2 - \phi^2)}$$

$$\text{Depth of crack} \quad h = w^2 - (R - b)$$

$$C_{11} = \frac{F_1}{\pi R^2} \sqrt{\pi h} \left(P_1 \left(\frac{h}{w} \right) \right), \quad C_{12} = \frac{2F_2}{\pi R^4} \times w \sqrt{\pi h} \left(P_2 \left(\frac{h}{w} \right) \right) \tag{2}$$

The expressions $P_1(h/w)$ and $P_2(h/w)$ are the experimental determined functions. The stress intensity factors C_{11} and C_{12} can be calculated using two experimental determined functions. So, the following two expressions can be represented as given below

$$P_1 \left(\frac{h}{w} \right) = \left(\frac{2w}{\pi h} \tan \left(\frac{\pi h}{2w} \right) \right)^{0.5} \left\{ \frac{0.752 + 2.02(h/w) + 0.37(1 - \sin(\pi h/2w)^3}{\cos(\pi h/2w)} \right\} \tag{3}$$

$$P_2 \left(\frac{h}{w} \right) = \left(\frac{2w}{\pi h} \tan \left(\frac{\pi w}{2h} \right) \right)^{0.5} \left\{ \frac{0.923 + 0.199(1 - \sin(\pi h/2w)^4}{\cos(\pi h/2w)} \right\} \tag{4}$$

Let V_t represent total strain energy due to fracture. Then, additional longitudinal displacement along the force F_i with the aid of Castiglione's theorem can be represented as follows

$$v_i = \frac{\partial V_t}{\partial F_i} \tag{5}$$

The total strain energy

$$V_t = \int_0^h \frac{\partial V_t}{\partial h} \mathrm{d}h = \int_0^h J_e \mathrm{d}h \tag{6}$$

Here, $J_e = \frac{\partial V_t}{\partial h}$, where J_e is an energy density function.

From equations (1), (5), and (6), we have

$$v_i = \frac{\partial}{\partial F_i} \left[\int_0^h J_e(h) \mathrm{d}h \right] \tag{7}$$

The flexibility influence coefficient (S_{ij}) in both X and Y directions can be obtained using equation (7).

$$S_{ij} = \frac{\partial v_i}{\partial F_j} = \frac{\partial^2}{\partial F_i \partial F_j} \int_0^h J_e(h) \mathrm{d}h \tag{8}$$

Integrating over the whole width of the crack from $-a$ to $+a$

$$S_{ij} = \frac{1 - \gamma^2}{E} \frac{\partial^2}{\partial F_i \partial F_j} \int_0^h \int_{-a}^a (C_{11} + C_{12})^2 \, \mathrm{d}\phi \mathrm{d}h \tag{9}$$

The combined equations (2), (3), (4), and (9) in the dimensionless form yield

$$\bar{S}_{11} = \frac{\pi ERS_{11}}{1 - \gamma^2} = 4 \int_0^{\bar{h}} \int_0^{\bar{a}} \bar{h} F_1^2(\bar{h}) \mathrm{d}\bar{\phi} \mathrm{d}\bar{h} \tag{10a}$$

$$\bar{S}_{21} = \bar{S}_{12} = \frac{\pi ER^2 S_{12}}{1 - \gamma^2} = 16 \int_0^{\bar{h}} \int_0^{\bar{a}} \bar{h} \sqrt{(1 - \bar{\phi}^2)} \times F_1(\bar{h}) F_2(\bar{h}) \mathrm{d}\bar{\phi} \mathrm{d}\bar{h} \tag{10b}$$

$$\bar{S}_{22} = \frac{ER^3 S_{22}}{1 - \gamma^2} = 64 \int_0^{\bar{h}} \int_0^{\bar{a}} \bar{h}(1 - \bar{\phi}^2) \times F_2^2(\bar{h}) \mathrm{d}\bar{\phi} \mathrm{d}\bar{h} \tag{10c}$$

where $\bar{h} = \frac{h}{R}, \quad \beta = \frac{h}{w}, \quad \bar{\phi} = \frac{\phi}{R}, \quad \bar{a} = \frac{a}{R}$

By taking the inverse of compliance matrix S_{ij}, the local stiffness matrix C_{ij} can be determined as presented in the following equation

$$C = \begin{bmatrix} C_{11} & C_{12} \\ C_{21} & C_{22} \end{bmatrix} = \begin{bmatrix} S_{11} & S_{12} \\ S_{21} & S_{22} \end{bmatrix}^{-1} \tag{11}$$

The stiffness matrix for the first and second crack location (Figure 3) can be obtained as follows.

First crack location

$$\bar{C} = \begin{bmatrix} \bar{C}_{11} & \bar{C}_{12} \\ \bar{C}_{21} & \bar{C}_{22} \end{bmatrix} = \begin{bmatrix} \bar{S}_{11} & \bar{S}_{12} \\ \bar{S}_{21} & \bar{S}_{22} \end{bmatrix}^{-1} \tag{12}$$

Second crack location

$$\bar{\bar{C}} = \begin{bmatrix} \bar{\bar{C}}_{11} & \bar{\bar{C}}_{12} \\ \bar{\bar{C}}_{21} & \bar{\bar{C}}_{22} \end{bmatrix} = \begin{bmatrix} \bar{\bar{S}}_{11} & \bar{\bar{S}}_{12} \\ \bar{\bar{S}}_{21} & \bar{\bar{S}}_{22} \end{bmatrix}^{-1} \tag{13}$$

Variation of dimensionless compliance with respect to nondimensional crack depth β is shown in Figure 4. It indicates that the dimensionless compliance increases with increasing nondimensional crack depth.

Formulation of mode shape and displacement for the cracked shaft

A steel shaft of length "L", diameter "D" with two cracks of depth b_1 and b_2 are taken at a distance of L_1 and L_2 from one of the fixed end. $v_1(x, t)$, $v_2(x, t)$, and $v_3(x, t)$ are the amplitudes of longitudinal vibration for the crack section-1, section-2, and section-3 (Figure 3), respectively. Similarly, the amplitude of bending vibration are $y_1(x, t)$, $y_2(x, t)$, and $y_3(x, t)$ at the corresponding section.
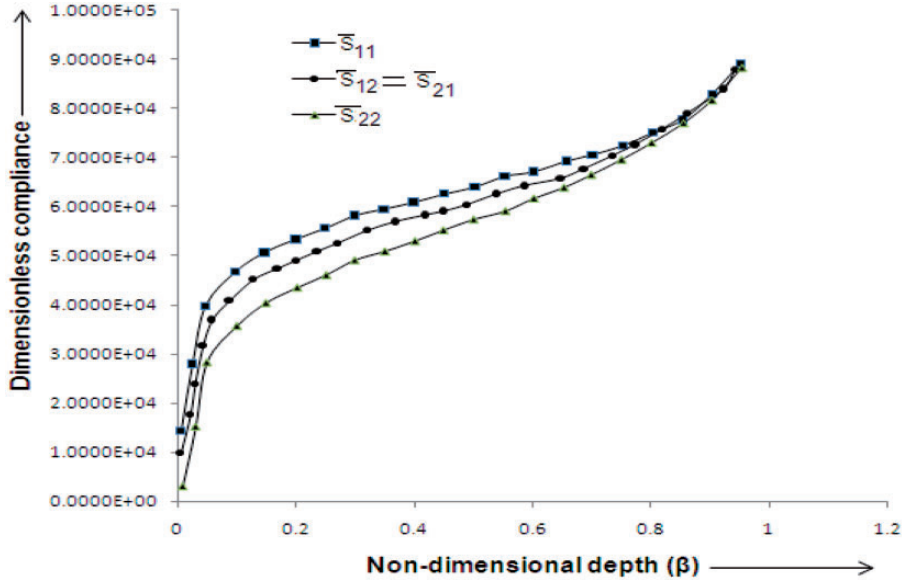
Figure 4. Dimensionless compliance ($\overline{S}_{i=12j=12}$) versus nondimensional crack depth (β).

The normal function for longitudinal and bending vibration of following crack sections for the given shaft can be expressed in nondimensional form as follows

$$\bar{v}_1(\bar{x}) = A_1 \cos(\bar{C}_v\bar{x}) + A_2 \sin(\bar{C}_v\bar{x}) \tag{14}$$

$$\bar{v}_2(\bar{x}) = A_3 \cos(\bar{C}_v\bar{x}) + A_4 \sin(\bar{C}_v\bar{x}) \tag{15}$$

$$\bar{v}_3(\bar{x}) = A_5 \cos(\bar{C}_v\bar{x}) + A_6 \sin(\bar{C}_v\bar{x}) \tag{16}$$

$$\bar{y}_1(\bar{x}) = A_7 \cosh(\bar{C}_y\bar{x}) + A_8 \sinh(\bar{C}_y\bar{x}) + A_9 \cos(\bar{C}_y\bar{x}) + A_{10} \sin(\bar{C}_y\bar{x}) \tag{17}$$

$$\bar{y}_2(\bar{x}) = A_{11} \cosh(\bar{C}_y\bar{x}) + A_{12} \sinh(\bar{C}_y\bar{x}) + A_{13} \cos(\bar{C}_y\bar{x}) + A_{14} \sin(\bar{C}_y\bar{x}) \tag{18}$$

$$\bar{y}_3(\bar{x}) = A_{15} \cosh(\bar{C}_y\bar{x}) + A_{16} \sinh(\bar{C}_y\bar{x}) + A_{17} \cos(\bar{C}_y\bar{x}) + A_{18} \sin(\bar{C}_y\bar{x}) \tag{19}$$

where $\bar{x} = \frac{x}{L}, \bar{v} = \frac{v}{L}, \bar{y} = \frac{y}{L}, \alpha_1 = \frac{L_1}{L}, \alpha_2 = \frac{L_2}{L}$ (Non − dimensional crack location)

$$\bar{C}_v = \frac{\omega L}{C_v}, \quad \bar{S}_v = \left(\frac{E}{\rho}\right)^{1/2}, \quad \bar{C}_y = \left(\frac{\omega L^2}{S_y}\right)^{1/2}, \quad S_y = \left(\frac{EI}{\mu}\right)^{1/2}, \quad \mu = A\rho$$

Boundary conditions are applied to determine 18 constants $A_i(i = 1, 2, 3 \ldots 18)$.
Considering the following boundary conditions of the cantilever shaft for four positions:

$$\text{At fixed end} \quad \bar{v}_1(0) = 0; \quad \bar{y}_1(0) = 0; \quad \bar{y}_1'(0) = 0$$
$$\text{At free end} \quad \bar{v}_3'(1) = 0; \quad \bar{y}_3'(1) = 0; \quad \bar{y}_3''(1) = 0$$

At first crack location
$$\bar{v}_1'(\alpha_1) = \bar{v}_2'(\alpha_1); \quad \bar{y}_1(\alpha_1) = \bar{y}_2(\alpha_1); \quad \bar{y}_1''(\alpha_1) = \bar{y}_2''(\alpha_1); \quad \bar{y}_1'''(\alpha_1) = \bar{y}_2'''(\alpha_1)$$

At second crack location
$$\bar{v}_2'(\alpha_2) = \bar{v}_3'(\alpha_2); \quad \bar{y}_2(\alpha_2) = \bar{y}_3(\alpha_2); \quad \bar{y}_2''(\alpha_2) = \bar{y}_3''(\alpha_2); \quad \bar{y}_2'''(\alpha_2) = \bar{y}_3'''(\alpha_2)$$

Because of discontinuity at crack location due to axial deformation at left and right of the first crack location can be obtained by force balancing. The given expression can be written as

$$AE\frac{dv_1(L_1)}{dx} = C_{11}(v_2(L_1) - v_1(L_1)) + C_{12}\left(\frac{dy_2(L_1)}{dx} - \frac{dy_1(L_1)}{dx}\right) \quad (20)$$

On multiplying equation (20) by a factor $AE/LC_{11}C_{12}$ we get

$$M_1 M_2 \bar{v}_1'(\alpha_1) = M_2(\bar{v}_2(\alpha_1) - \bar{v}_1(\alpha_1)) + M_1\left(\bar{y}_2'(\alpha_1) - \bar{y}_1'(\alpha_1)\right) \quad (21)$$

Similarly due to discontunity of slope on either side of the first crack location, the moment balance can be applied. So the given equation takes the form of

$$EI\frac{d^2 y_1(L_1)}{dx^2} = C_{21}(v_2(L_1) - v_1(L_1)) + C_{22}\left(\frac{dy_2(L_1)}{dx} - \frac{dy_1(L_1)}{dx}\right) \quad (22)$$

On multiplying equation (22) by a factor $EI/L^2 C_{22}C_{21}$, we get

$$M_3 M_4 \bar{y}_1''(\alpha_1) = M_3(\bar{v}_2(\alpha_1) - \bar{v}_1(\alpha_1)) + M_4\left(\bar{y}_2'(\alpha_1) - \bar{y}_1'(\alpha_1)\right) \quad (23)$$

where, $M_1 = \frac{AE}{LC_{11}}$, $M_2 = \frac{AE}{C_{12}}$, $M_3 = \frac{AI}{LC_{22}}$, $M_4 = \frac{EI}{L^2 C_{21}}$

Similarly, by applying force and moment balance to the second crack section (L_2), the following expression can be derived

$$M_5 M_6 \bar{v}_2'(\alpha_2) = M_6(\bar{v}_3(\alpha_2) - \bar{v}_2(\alpha_2)) + M_5(\bar{y}_3'(\alpha_2) - \bar{y}_2'(\alpha_2)) \quad (24)$$

$$M_7 M_8 \bar{y}_2''(\alpha_2) = M_7(\bar{v}_3(\alpha_2) - \bar{v}_2(\alpha_2)) + M_8\left(\bar{y}_3'(\alpha_2) - \bar{y}_2'(\alpha_2)\right) \quad (25)$$

where, $M_5 = \frac{AE}{LC_{11}}$, $M_6 = \frac{AE}{C_{12}}$, $M_7 = \frac{EI}{LC_{22}}$, $M_8 = \frac{EI}{L^2 C_{21}}$

The normal functions from equations (14) to (19) with the boundary conditions at four locations as mentioned above, rise to the characteristic equation of given the system as

$$|R| = 0$$

where R is a 18×18 matrix. The determinant of the given matrix is a function of natural frequency (ω), nondimensional crack location (α_1, α_2), and the local stiffness matrix "C". Again local stiffness matrix is the function of nondimensional crack depth (β_1 and β_2).

Various results of the theoretical analysis have been generated taking different crack sections with physical property of the same shaft as given in Table 3 for uncracked and cracked shaft. Some of the examples of theoretical results are given in Table 1. Effect of crack location and depth on eigenvalues have been plotted as shown in Figure 5(a) to (c).

The elements of the *R*-matrix are as follows.

$$R_1 = \cosh(\overline{c_y}\alpha_1), \ R_2 = \sin h(\overline{c_y}\alpha_1), \ R_3 = \cosh(\overline{c_y}), \ R_4 = \sin h(\overline{c_y}), \ R_5 = \cos(\bar{c}_y\alpha_1),$$
$$R_6 = \sin(\bar{c}_y\alpha_1), \ R_7 = \cos(\bar{c}_y), \ R_8 = \sin(\bar{c}_y), \ R_{10} = \sinh(\bar{c}_y\alpha_2), \ K_{14} = -M_{12}\bar{c}_yR_1,$$
$$R_9 = \cos h(\bar{c}_y\alpha_2), \ K_3 = -R_6 - M_3\bar{c}_yR_5, \ R_{11} = \cos(\bar{c}_y\alpha_2), \ R_{12} = \sin(\bar{c}_y\alpha_2),$$
$$T_5 = \cos(\bar{c}_y\alpha_1), \ T_7 = \cos(\bar{c}_y), \ T_6 = \sin(\bar{c}_y\alpha_1), \ T_8 = \sin(\bar{c}_y), \ T_9 = \cos(\bar{c}_y\alpha_2),$$
$$T_{10} = \sin(\bar{c}_y\alpha_2), \ M_{12} = M_1/M_2, \ M_{34} = M_3/M_4, \ M_{56} = M_5/M_6, \ M_{78} = M_7/M_8,$$

$$K_1 = R_2 + M_3\bar{c}_yR_1, \ K_2 = R_1 + M_3\bar{c}_yR_2, \ K_4 = -R_5 - M_3\bar{c}_yR_6, \ K_5 = \frac{M_{34}}{\bar{c}_y} \times T_5,$$

$$K_6 = \frac{M_{34}}{\bar{c}_y} \times T_6, \ K_7 = \frac{-M_{34}}{\bar{c}_y} \times T_5, \ K_8 = \frac{-M_{34}}{\bar{c}_y} \times T_6, \ K_9 = M_{12}\bar{c}_yR_2, \ K_{10} = M_{12}\bar{c}_yR_1,$$

$$K_{11} = -M_{12}\bar{c}_yR_6, \ K_{12} = M_{12}\bar{c}_yR_5, \ K_{13} = -M_{12}\bar{c}_yR_2, \ K_{15} = M_{12}\bar{c}_yR_6, \ K_{16} = -M_{12}\bar{c}_yR_5,$$
$$K_{17} = T_5 - M_1\bar{c}_yT_6, \ K_{18} = T_6 + M_1\bar{c}_yT_5, \ KK_1 = R_{10} + M_7\bar{c}_yR_9, \ KK_2 = R_9 + M_7\bar{c}_yR_{10},$$

$$KK_3 = -R_{12} - M_7\bar{c}_yR_{11}, \ KK_4 = -R_{11} - M_7\bar{c}_yR_{12}, \ KK_5 = \frac{M_{78}}{\bar{c}_y}T_9, \ KK_6 = \frac{M_{78}}{\bar{c}_y}T_{10},$$

$$KK_7 = \frac{-M_{78}}{\bar{c}_y}T_9, \ KK_8 = \frac{-M_{78}}{\bar{c}_y}T_{10}, \ KK_9 = M_{56}\bar{c}_yK_{10}, \ KK_{10} = M_{56}\bar{c}_yK_9,$$

$$KK_{11} = -M_{56}\bar{c}_yR_{12}, \ KK_{12} = M_{56}\bar{c}_yR_{11}, \ KK_{13} = -M_{56}\bar{c}_yR_{10}, \ KK_{14} = -M_{56}\bar{c}_yR_9,$$
$$KK_{15} = M_{56}\bar{c}_yR_{12}, \ KK_{16} = -M_{56}\bar{c}_yR_{11}, \ KK_{17} = T_9 - M_5\bar{c}_yT_{10}, \ KK_{18} = T_{10} + M_5\bar{c}_yT_9,$$

R-Matrix

0	1	0	0	0	0	0	0	0	0	0	0	0	0	0	0	0	0
1	0	1	0	0	0	0	0	0	0	0	0	0	0	0	0	0	0
0	0	0	0	0	0	0	R_3	R_4	$-R_7$	$-R_8$	0	0	0	0	0	0	0
0	0	0	0	0	0	0	R_4	R_3	R_8	$-R_7$	0	0	0	0	0	0	R_7
R_2	$-R_5$	$-R_6$	$-R_1$	$-R_2$	R_5	R_6	0	0	0	0	0	0	0	0	0	0	0
R_1	R_6	$-R_5$	$-R_2$	$-R_1$	$-R_6$	R_5	0	0	0	0	0	0	0	0	0	0	0
R_2	R_5	R_6	$-R_1$	$-R_2$	$-R_5$	$-R_6$	0	0	0	0	0	0	0	0	0	0	0
0	0	0	R_9	R_{10}	$-R_{11}$	$-R_{12}$	$-R_9$	$-R_{10}$	R_{11}	R_{12}	0	0	0	0	0	0	0
0	0	0	R_{10}	R_9	R_{12}	$-R_{11}$	$-R_{10}$	$-R_9$	$-R_{12}$	R_{11}	0	0	0	0	0	0	0
0	0	0	R_9	R_{10}	R_{11}	R_{12}	$-R_9$	$-R_{10}$	$-R_{11}$	$-R_{12}$	0	0	0	0	0	0	0
K_2	K_3	K_4	$-R_2$	$-R_1$	R_9	$-R_5$	0	0	0	0	K_5	K_6	K_7	K_8	0	0	$-T_9$
0	0	0	KK_1	KK_2	KK_3	KK_4	$-R_{10}$	$-R_9$	R_{12}	$-R_{11}$	0	0	KK_5	KK_6	KK_7	KK_8	0
0	0	0	0	0	0	0	0	0	0	0	1	0	0	0	0	0	0
0	0	0	0	0	0	0	0	0	0	0	0	0	0	0	$-T_8$	$-T_7$	0
0	0	0	0	0	0	0	0	0	0	0	$-T_6$	$-T_5$	T_6	$-T_5$	0	0	0
0	0	0	0	0	0	0	0	0	0	0	0	0	$-T_{10}$	T_9	T_{10}	$-T_9$	0
K_{10}	K_{11}	K_{12}	K_{13}	K_{14}	K_{15}	K_{16}	0	0	0	0	K_{17}	K_{18}	$-T_5$	$-T_6$	0	0	$-T_{10}$
0	0	0	KK_9	KK_{10}	KK_{11}	KK_{12}	KK_{13}	KK_{14}	KK_{15}	KK_{16}	0	0	KK_{17}	KK_{18}	$-T_9$	$-T_{10}$	KK_6

R-Matrix

Table 1. Some of the results of theoretical analysis.

Sl. No.	1st Crack location (α_1)	1st Crack depth (β_1)	2nd Crack location (α_2)	2nd Crack depth (β_2)	Relative 1st natural frequency (lnf)	Relative 2nd natural frequency (mnf)	Relative 3rd natural frequency (fnf)	Relative 1st mode shape difference (amd)	Relative 2nd mode shape difference (bmd)	Relative 3rd mode shape difference (cmd)
1	0.1	0.1	0.8	0.1	0.9989	0.9998	0.9979	0.0348	0.0174	0.0212
2	0.15	0.125	0.8	0.1	0.9895	0.9989	0.9879	0.0545	0.0104	0.0199
3	0.2	0.15	0.8	0.1	0.9795	0.9867	0.9859	0.0696	.01456	0.0361
4	0.25	0.175	0.8	0.1	0.9784	0.9987	0.9793	0.0850	0.0069	0.0823
5	0.3	0.2	0.8	0.1	0.9697	0.9943	0.9728	0.1024	0.0313	0.1434
6	0.35	0.225	0.8	0.1	0.9745	0.9949	0.9891	0.1141	0.0905	0.1683
7	0.4	0.25	0.8	0.1	0.9898	0.9981	0.9872	0.1012	0.1811	0.1321
8	0.45	0.275	0.8	0.1	0.9762	0.9892	0.9993	0.1024	0.2961	0.0548
9	0.5	0.3	0.8	0.1	0.9585	0.9893	0.9981	0.0915	0.4181	0.0137
10	0.55	0.325	0.8	0.1	0.9784	0.9894	0.9984	0.0806	0.5261	0.1022
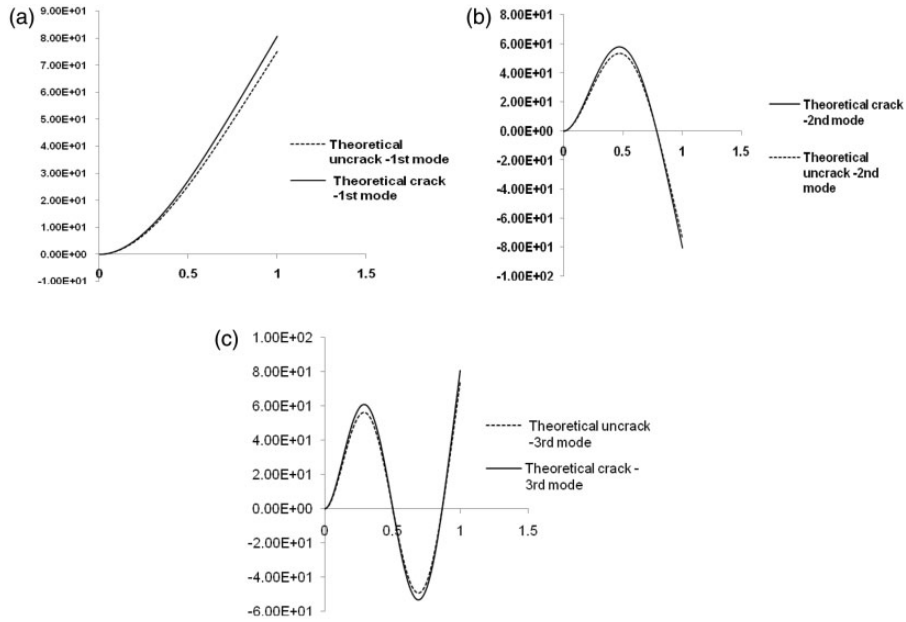
Figure 5. (a) Nondimensional amplitude vs. nondimensional distance from the hinge end (first mode of vibration) $\alpha_1 = 0.2$, $\alpha_2 = 0.8$, $\beta_1 = 0.1$, $\beta_2 = 0.1$; (b) nondimensional amplitude vs. nondimensional distance from the hinge end (second mode of vibration) $\alpha_1 = 0.2$, $\alpha_2 = 0.8$, $\beta_1 = 0.1$, $\beta_2 = 0.1$; (c) nondimensional amplitude vs. nondimensional distance from the hinge end (third mode of vibration) $\alpha1 = 0.2$, $\alpha2 = 0.8$, $\beta1 = 0.1$, $\beta2 = 0.1$.
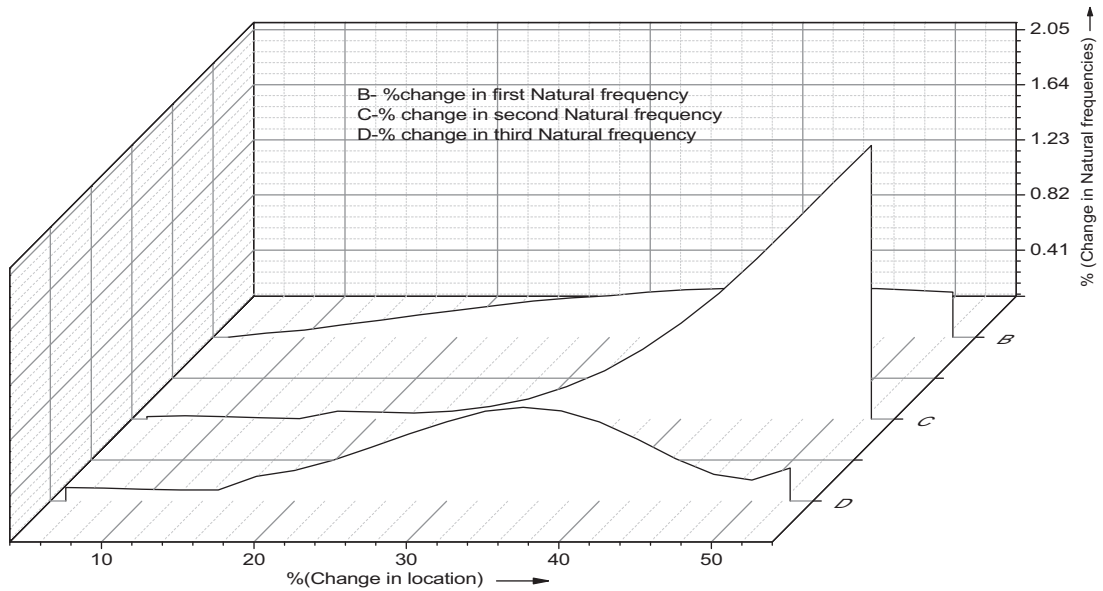
Figure 6. Percentage change in natural frequencies vs. percentage change in first crack location from the hinge end, $\beta_1 = 0.1$, $\beta_2 = 0.1$, $\alpha_2 = 0.8$.
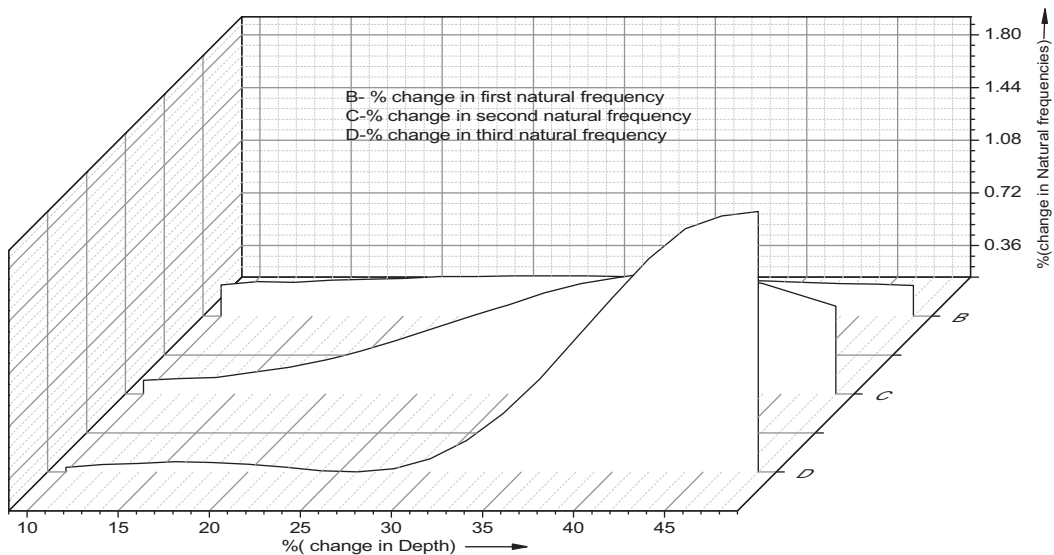
Figure 7. Percentage change in natural frequencies vs. percentage change in depth $\alpha_1 = 0.2$, $\alpha_2 = 0.75$, $\beta_1 = \beta_2 = 10\% \ldots 48\%$.

ANFIS methodology

ANFIS stands for adaptive neuro-fuzzy inference system and was developed by Jang (1997). It is a feed-forward ANN, which are functionally equivalent to fuzzy inference systems. He reported that the ANFIS architecture can be employed to model nonlinear functions, nonhomogeneous, and complex fuctions. It is a hybrid neuro-fuzzy technique that brings learning capabilities of neural networks to fuzzy inference systems and uses hybrid learning algorithm. It is a part of the fuzzy logic toolbox in MATLAB R2008a software of Math Work Inc. (1995–1998). Jang et al. (1997) and Avci (2008) reported fuzzy inference system (FIS), which is used to compute framework based on the concepts of fuzzy set theory, fuzzy if–then rule, and fuzzy reasoning. The application of ANFIS has been successfully found in in the fields of forecasting stock market short-term trends (Atsalakis and Valavanis, 2009) and comparision of wavelet families for texture classification (Avci, 2008). The basic components of an FIS consists of three conceptual processes: fuzzification—which translate input parameters into truth values; rule evaluation—which compute output truth values; defuzzification—which transfer truth values into output. The FIS that have been considered in this paper maps: input characteristics to input membership functions, input membership function to rules, rules to a set of output characteristics, output characteristics to output membership functions, and output membership function to single valued output.

For solving the influence of multi-crack with location and size due to transverse loading presented in this paper, the Sugeno fuzzy inference system is used to obtain the fuzzy model. The Sugeno FIS was proposed by Takagi et al. (1988, 1985) in an effort to develop a systematic approach to generate fuzzy rules from a given input and output data set. The first, second, and third natural frequencies obtained from theoretical analysis in this paper are used as training data to train ANFIS network with Gussian membership function with a hybrid learning algorithm. In this paper, the ANFIS structure with first-order Sugeno model consists of 27 rules are considered. For the neuro-fuzzy
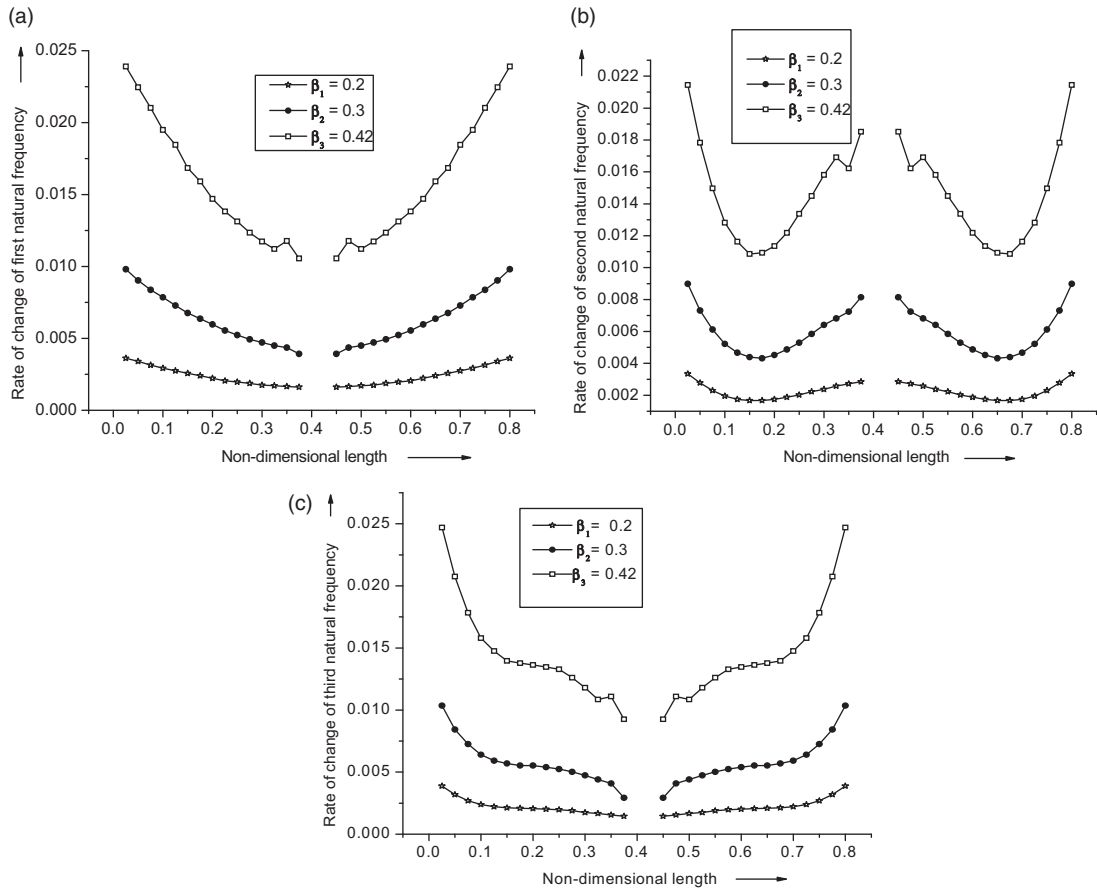
Figure 8. (a) Rate of change in first natural frequencies vs. nondimensional length $\alpha_1 = 0.025 \ldots 0.4$, $\alpha_2 = 0.8 \ldots 0.45$, $\beta_1 = 0.2$, $\beta_2 = 0.3$, $\beta_3 = 0.42$; (b) rate of change in second natural frequencies vs. nondimensional length $\alpha_1 = 0.025 \ldots 0.4$, $\alpha_2 = 0.8 \ldots 0.45$, $\beta_1 = 0.2$, $\beta_2 = 0.3$, $\beta_3 = 0.42$; (c) rate of change in third natural frequencies vs. nondimensional length $\alpha_1 = 0.025 \ldots 0.4$, $\alpha_2 = 0.8 \ldots 0.45$, $\beta_1 = 0.2$, $\beta_2 = 0.3$, $\beta_3 = 0.42$.

model used in this work, of the 10 data points obtained using theoretical analysis, 7 are used for training and the remaining 3 are used for testing (or validating). Training of ANFIS is usually performed by using ANFIS Editor GUI of MATLAB (2000). The ANFIS Editor GUI window displays the four main sub-displays.

These are:

(1) Load data,
(2) Generate FIS,
(3) Train FIS and
(4) Test FIS. Once the FIS is generated, the model structure can be viewed as shown in Figure 9.

The ANFIS information used in this work is tabulated in Table 2.
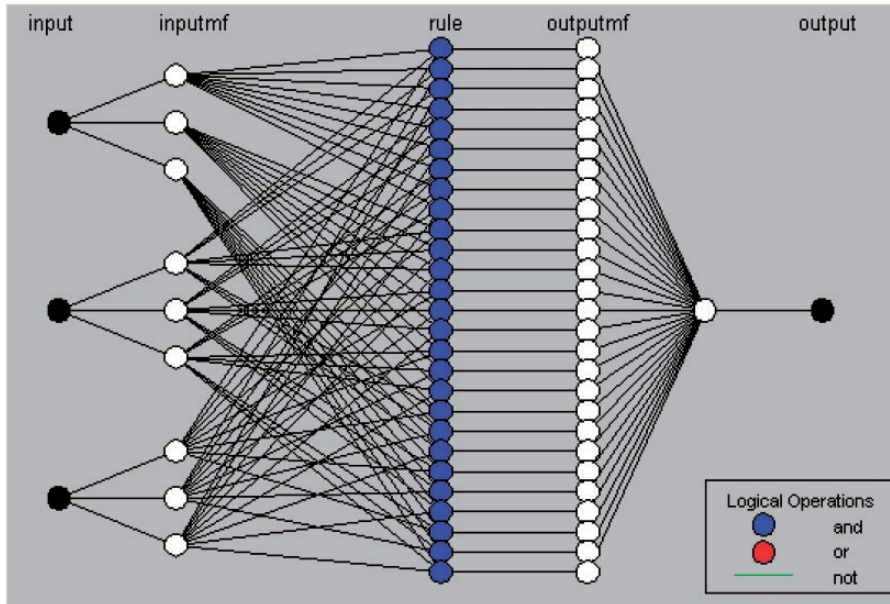
Figure 9. ANFIS model structure for the influence of multi-crack with location and size due to transverse loading.
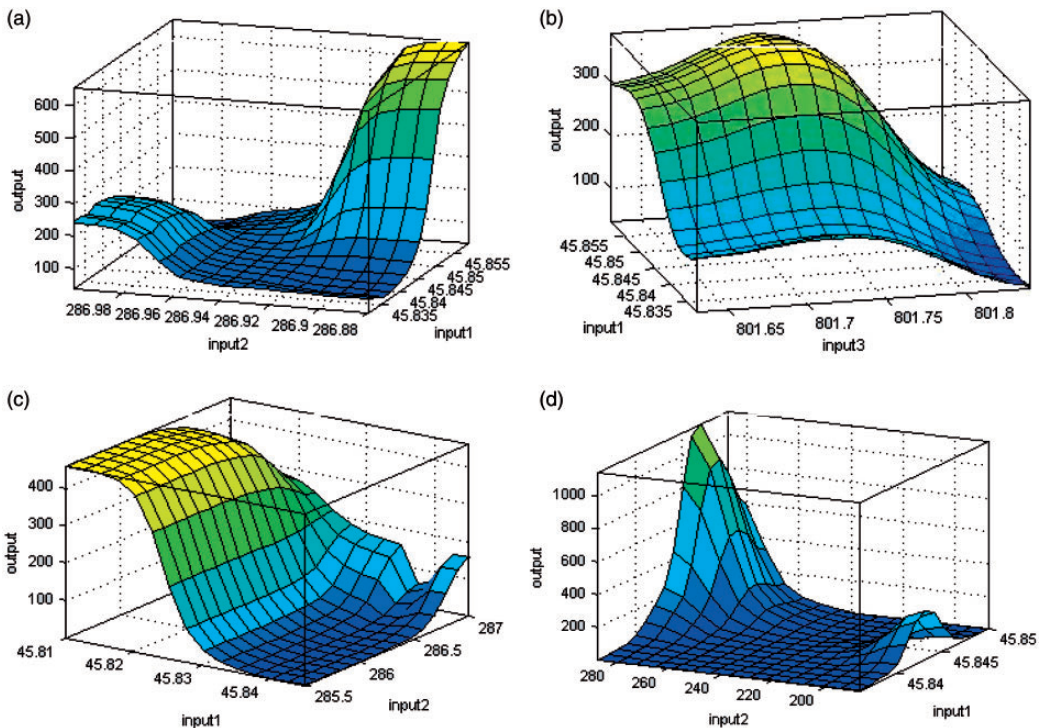
Figure 10. Surface plot of 1st and 2nd crack location and crack depth. (a) For 2nd crack depth; (b) for 2nd crack location; (c) for 1st crack location; (d) for 1st crack depth.

Table 2. ANFIS information used for solving 7-DOF redundant manipulator.

Three inputs	1st, 2nd, and 3rd natural frequencies
One output	Crack location and crack depth
Three membership function in each node	Sugeno types
Number of nodes	78
Number of linear parameters	27
Number of nonlinear parameters	27
Total number of parameters	54
Number of training data pairs	7
Number of checking data pairs	10
Number of fuzzy rules used	27

Results and discussion

In this section, surface plots, the residual plots, and the normal probability plots are carried out to obtain the theoretical results. The surface plot obtained explains the efficiency of the ANFIS methodology. The residual plots obtained by comparing the predicted data from the ANFIS and the theoretical data show that the data predicted using ANFIS methodology deviate very less from the theoretical data. The last section of this chapter is concluded with obtaining the normal probability plots. The details of the plots are explained in the following section.

3D Surface viewer analysis

In this section, the 3D surface plots obtained from the natural frequency of the shaft with its various crack positions and sizes are discussed. The surface plots display both the connecting lines and aces of the surface in color. The 3D surface plots obtained from ANFIS explains the relation between the output and two inputs. Figure 10(a) to (d) shows surface plots for four ANFIS networks relating inputs to crack locations and depths. This section shows the obtained surface plots of different crack locations; similarly, the surface plots for different crack depths can be obtained. It can be concluded from the surface plot that the contribution of interdependent parameters toward obtaining the output can be easily provided through the ANFIS algorithm and can be hardly obtained otherwise without employing massive computations. The surface viewer plots show that the total surface is covered by rule base.

Residual plot analysis

Residuals are the difference between the predicted output from the ANFIS model and the actual values of natural frequencies. The residual plot is a graph that shows the errors in vertical axis and the indepandant variables in the horizontal axis. If the errors in the residual plot are randomly dispersed around the horizontal axis, then the predicted model is considerd to be suitable for the given data, i.e. there is no drift in the data. In this section, the residual plots are obtained for training and testing data for different conditions. Figure 11(a) and (b) indicates a decent fit to the model of different crack locations, as most of the residual lies between −0.02 and 0.02. Similarly, the residual plots of rest crack location and crack depth can also be obtained.

Figure 11. Residual plot of training data of: (a) 2nd and (b) 1st location.
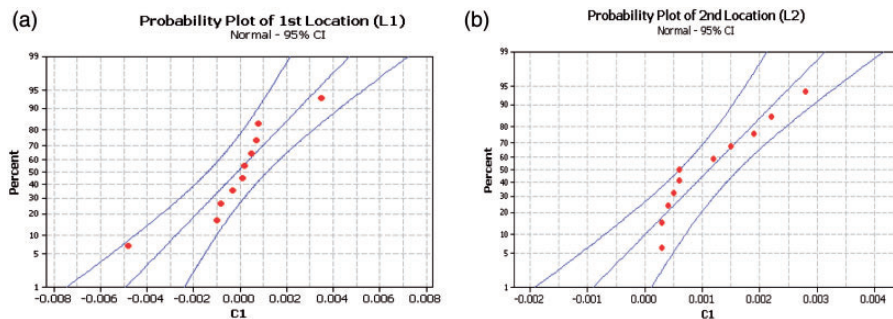
Figure 12. (a) Normal probability plot for 1st location; (b) normal probability plot for 2nd location.

Normal probability plot analysis

The normal probability plot developed by Chambers et al. (1983) is a graphical method for assessing whether or not a data is approximately normally distributed, if it is nearly straight, the data satisfy the nearly normal condition. The data are plotted against a theoretical normal distribution in such a way that the points should form an approximate straight line. Any deviation from this straight line indicates a deviation from the normality. It provides a good assessment of the adequacy of the normal model for a set of data. In this plot, the normal distribution is represented by a straight line angled at $45°$. In this section, normal probability plot for two crack locations is presented as shown in Figure 12(a) and (b). The figure suggests that all the data are normally distributed. Similarly, the normal probability for all training and testing data of rest crack location and crack depth are obtained and the plot signifies that the data are normally distributed.

Experimental set-up

Experimental analysis is carried out by measuring the dynamic response of the uncracked and cracked mild steel shaft specimen. The material properties of the shaft are given in Table 3. The cracks at various locations with different depths in the shafts were introduced by electro-discharge machine perpendicular to the longitudinal axis of the shaft. The test specimen made up of mild steel is 1000 mm length and 10 mm diameter. The cantilever shaft test sample was clamped at its one end by a clamping device. The free end of the shaft specimen was excited by an appropriate signal from the function generator, which was amplified by the amplifier. The cantilever shaft was excited at first three modes of vibration, and the natural frequencies and mode shapes were recorded by the hardware support accordingly, i.e. miniature accelerometer by suitable positioning, data acquisition

Table 3. Material properties and geometry of structural steel shaft.

Young's modulus of shaft, E	Density of shaft, ρ	Poisson's ratio of shaft, μ	Length of shaft, L	Diameter of shaft, D
2.1 E + 06 MPa	7830 kg/m^3	0.3	1000 mm	10 mm

1. Steel Cantilever shaft   2. Vibration Exciter   3. Power amplifier
4. Function Generator   5. Distribution box   6. supply of power
7. Vibrationindicator   8. Vibration Analyzer   9. Accelerometer
10. Software (NV Gate Envirnoment software)
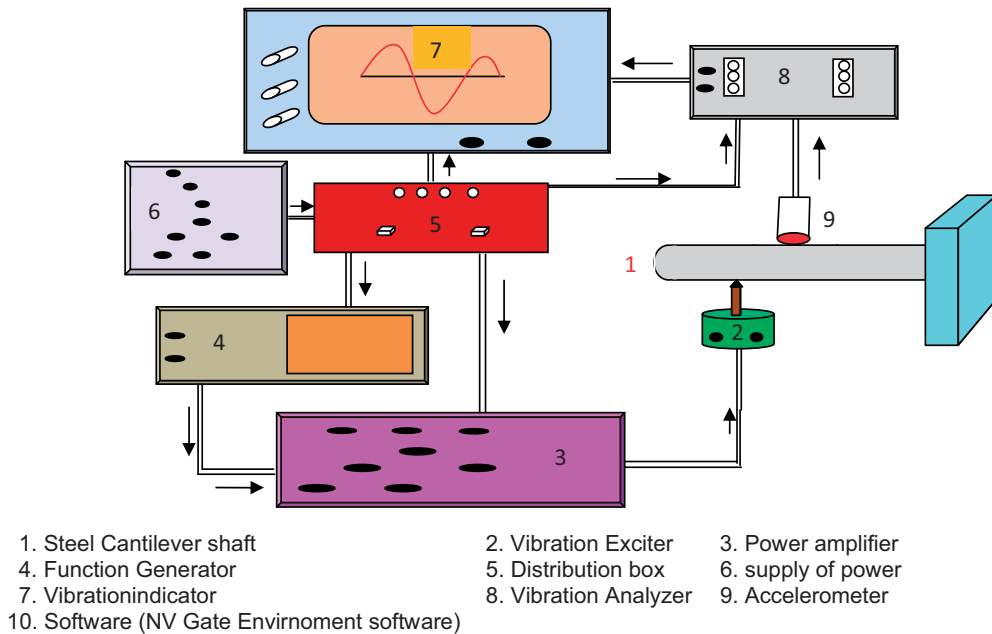
Figure 13. Experimental setup.

system, and tuning the vibration generator at the corresponding resonant frequencies. Finally, the analysis of the vibration parameters from the intact and cracked shafts were done by the NVgate Environment Software loaded on the laptop of the vibration analyzer. The schematic diagram of experimental setup is shown in Figure 13. Some of the useful instruments are given in Figure 14(a) to (d). Results for the first three nondimensional amplitude along nondimensional length are plotted in Figure 15(a) to (c).

$$\%\,\text{Error} = \left| \frac{\%\,\text{Change in Experimental Natural Frequency} - \%\,\text{Change in Theoretical Natural Frequency}}{\%\,\text{Change in Experimental Natural Frequency}} \right|$$

Discussions

The following conclusion can be derived supporting the results from the theoretical analysis. The dimensionless compliances ($\bar{S}_{11}$, $\bar{S}_{12} = \bar{S}_{21}$, $\bar{S}_{22}$) increase with the increasing nondimensional crack

Figure 14. (a) Vibration indicator (NVgate Envirnoment software); (b) cantilever shaft with frame; (c) vibration analyzer; (d) vibration pick-up with shaft.

depth as shown in Figure 4. First three mode shapes are reflected graphically in Figure 5(a) to (c) for different nondimensional crack locations and nondimensional crack depths. It is observed that there are changes in mode shapes at different locations and depths due to the presence of crack in the shaft. Table 1 shows some of the nondimensional natural frequencies and mode shape differences obtained from theoretical analysis with their location and depth. Figure 6 illustrates the percentage change in the fundamental frequency of the cantilever steel shaft with two cracks as a function of percentage change in first crack location with two fixed crack depths. The second natural frequency increases rapidly in comparison to first and third natural frequencies as the first crack moves from fixed end towards the second crack location with constant crack depth. The effect of crack depth on modal values is shown in Figure 7. The third natural frequency increases rapidly at high crack depth ($0.35 < \beta < 0.5$). Figure 8(a) to (c) demonstrates the first, second, and third nondimensional natural frequencies as a function of nondimensional crack length for constant nondimensional crack depth. As the two cracks move towards each other, the first natural frequency decreases rapidly (Figure 8(a)) at higher crack depth ($\beta = 0.42$) in comparison to low crack depth ($\beta = 0.2$, $\beta = 0.3$). But in case of second natural frequency (Figure 8(b)), it decreases at low crack region ($0 < \beta < 0.2$) and increases at medium region crack ($0.2 < \beta < 0.35$). It is found that when two cracks location move towards each other, the third nondimensional frequency decreases continuously irrespective of depths
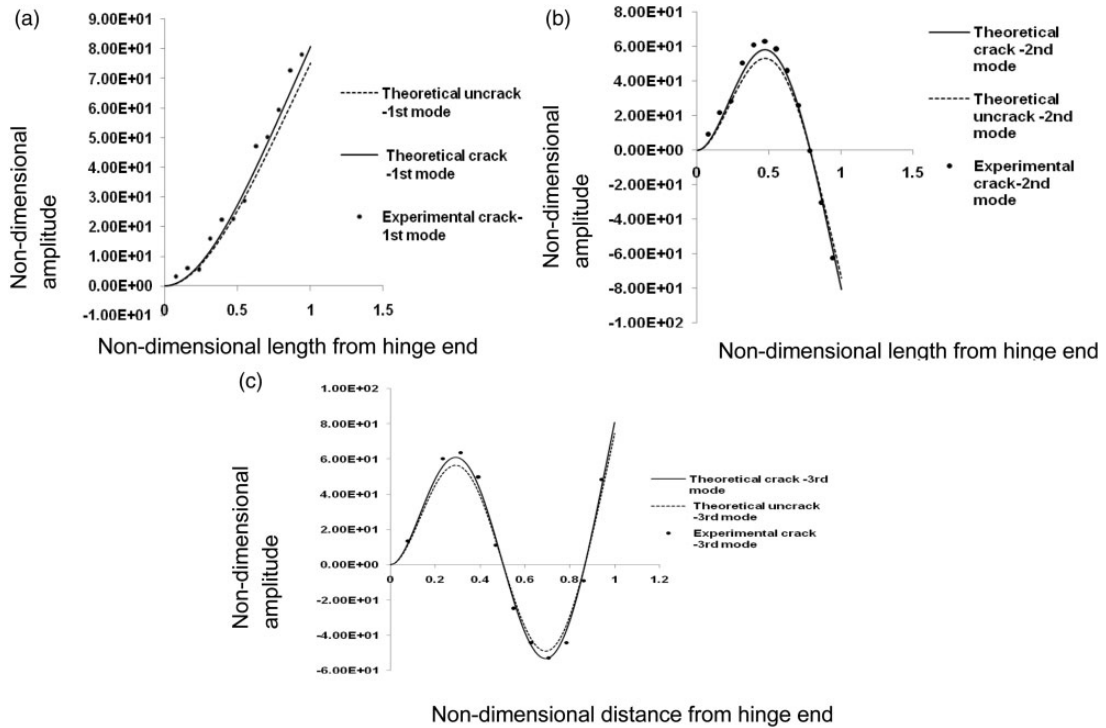
Figure 15. (a) Nondimensional amplitude vs. nondimensional length from hinge end (1st mode of vibration) $\alpha 1 = 0.01$, $\alpha 2 = 0.85$, $\beta 1 = 0.2$, $\beta 2 = 0.2$; (b) nondimensional amplitude vs. nondimensional length from the fixed end (2nd mode of vibration) $\alpha 1 = 0.01$, $\alpha 2 = 0.85$, $\beta 1 = 0.2$, $\beta 2 = 0.2$; (c) nondimensional amplitude vs. nondimensional distance from hinge end (3rd mode of vibration) $\alpha 1 = 0.01$, $\alpha 2 = 0.85$, $\beta 1 = 0.2$, $\beta 2 = 0.2$.

(Figure 8(c)). But the rate of decrease is steeper within the range $(0 < \beta < 0.2)$ as compared to the medium crack $(0.2 < \beta < 0.35)$. There is significant change in mode shape between theoretical cracked and uncrack shaft with experimental crack shaft as given in Figure 15(a) to (c). Table 4 shows a comparison of relative natural frequency obtained in theoretical and experimental analysis. The values shown in the table are approximately $\pm 7.33\%$ in-between the two analyses.

Conclusion

This paper approaches a clear representation of the position of two cracks with its location and depths on modal frequencies and mode shapes. The crack locations and its depths significantly influence the mode shapes and natural frequencies of the elastic structures. The rate of change in natural frequencies with its maximum amplitudes are observed at all three mode shapes specially at crack locations. These changes in natural frequencies and mode shapes will be helpful in forecasting the crack position with its intensity.The mode shapes for the cracked shaft obtained numerically are compared with the corresponding experimental results and are found to be in close agreement. The surface plots, the residual plots, and the normal probability plots obtained from ANFIS are validated with the theoretical results. The surface plots prove the efficiency of the ANFIS methodology. The residual plots are taken care by comparing the predicted data from the ANFIS and the

Table 4. Comparison between theoretical and experimental analyses.

Sl. No.	α_1 $(L_1)/L$	β_1 $(d_1)/D$	α_2 $(L_2)/L$	β_2 $(d_2)/D$	% Change in natural frequency—Theoretical analysis			% Change in natural frequency—Experimental analysis			% Error in natural frequency		
					Ω_1	Ω_2	Ω_3	Ω_4	Ω_5	Ω_6	1st	2nd	3rd
1	0.425	0.1	0.525	0.12	0.031	0.091	0.017	0.033	0.096	0.019	6.061	5.208	10.526
2	0.4	0.12	0.55	0.14	0.044	0.125	0.045	0.047	0.134	0.048	6.383	6.716	6.250
3	0.375	0.14	0.575	0.16	0.061	0.16	0.09	0.064	0.173	0.095	4.688	7.514	5.263
4	0.35	0.16	0.6	0.18	0.083	0.188	0.167	0.089	0.205	0.181	6.742	8.293	7.735
5	0.325	0.18	0.625	0.2	0.113	0.216	0.271	0.121	0.233	0.294	6.612	7.296	7.823
6	0.3	0.2	0.65	0.22	0.157	0.23	0.393	0.171	0.251	0.426	8.187	8.367	7.746
7	0.275	0.22	0.675	0.24	0.209	0.23	0.518	0.225	0.249	0.559	7.111	7.631	7.335
8	0.25	0.24	0.7	0.26	0.279	0.223	0.612	0.303	0.241	0.662	7.921	7.469	7.553
9	0.225	0.26	0.725	0.28	0.362	0.202	0.672	0.395	0.219	0.724	8.354	7.763	7.182
10	0.2	0.28	0.75	0.3	0.48	0.195	0.684	0.521	0.212	0.739	7.869	8.019	7.442
11	0.175	0.3	0.775	0.32	0.606	0.202	0.637	0.652	0.217	0.687	7.055	6.912	7.278
12	0.15	0.32	0.8	0.34	0.794	0.244	0.55	0.858	0.265	0.595	7.459	7.925	7.563
13	0.125	0.34	0.825	0.36	0.89	0.348	0.47	0.96	0.376	0.509	7.292	7.447	7.662
14	0.1	0.36	0.85	0.38	0.903	0.529	0.448	0.977	0.569	0.486	7.574	7.030	7.819
15	0.075	0.38	0.875	0.4	0.916	0.836	0.575	0.981	0.905	0.622	6.626	7.624	7.556
16	0.05	0.42	0.9	0.42	0.929	0.884	0.645	0.999	0.956	0.697	7.007	7.531	7.461

theoretical data. ANFIS part is concluded with the normal probability plots. The methodology can be utilized for condition monitoring of any vibrating structures. Studies can be extended to procreate new artificial intelligence technique for damage detection in structures.

Conflict of interest

None declared.

References

Atsalakis GS and Valavanis KP (2009) Forecasting stoke market short term trend using neuro-fuzzy based methodology. *Expert System with Applications* 36: 10696–10707.

Avci E (2008) Comparison of wavelet families for texture classification by using wavelet packet entropy adoptive network based fuzzy inference system. *Soft Computing* 8: 225–231.

Chambers J, Cleveland W, Kleiner B, et al. (1983) *Graphical Methods for Data Analysis*. Belmont, CA: Wadsworth.

Chandrashekhar M and Ganguli R (2009) Structural damage detection using modal curvature and fuzzy logic. *Structural Health Monitoring* 8(4): 0267–16.

Cheng YS and Tham LG (2003) Structural damage detection based on a micro-genetic algorithm using incomplete and noisy modal test data. *Journal of Sound & Vibration* 159: 1081–1094.

Dixit A and Hanagud S (2011) Single beam analysis of damaged beams verified using a strain energy based damage measure. *International Journal of Solids and Structures* 48: 592–602.

Edward M, Murphy Z, Kevin D, et al. (2011) Crack identification in a freely vibrating plate using Bayesian parameter estimation. *Mechanical Systems and Signal Processing* 25: 2125–2134.

Jang JSR, Sun CT and Mizutani E (1997) *Neuro-Fuzzy and Soft Computing*. New York: Prentice Hall.

Koivo H (2000) ANFIS: Adaptive neuro-fuzzy inference system. In: European symposium on intelligent technology, Aachen, Germany.

Liu GR, Nourbakhshnia N and Zhang YW (2011) A novel singular ES-FEM method for simulating singular stress fields near the crack tips for linear fracture problems. *Engineering Fracture Mechanics* 78: 863–876.

Lundmark P and Varna J (2011) Stiffness reduction in laminates at high intralaminar crack density: Effect of crack interaction. *International Journal of Damage Mechanics* 20(2): 279–297.

Movaghghar A and Lvov GI (2012) A method of estimating wind turbine blade fatigue life and damage using continuum damage mechanics. *International Journal of Damage Mechanics* 21: 810–821.

Nanda J and Das HC (2013) Fault diagnosis of steel cantilever beam with double crack using GA. *European Journal of Scientific Research* 96: 348–360.

Nanda J, Parhi DR and Das HC (2013) Theoretical analysis of the shaft: Advance in fuzzy system 1. Article ID 392470, p. 11.

Palmeri A and Cicirello A (2011) Physically-based Dirac's delta functions in the static analysis of multi-cracked Euler–Bernoulli and Timoshenko beams. *International Journal of Solids and Structures* 48: 2184–2195.

Panigrahi SK, Chakraverty S and Mishra BK (2004) Vibration based damage detection in a uniform strength beam using a genetic algorithm. *Meccanica* 44: 697–710.

Pham DC, Sun XS, Tan VBC, et al. (2012) Progressive failure analysis of scaled double-notched carbon/epoxy composite laminates. *International Journal of Damage Mechanics* 21: 1154–1185.

Rezaee M and Hassannejad R (2011) A new approach to free vibration analysis of a beam with a breathing crack based on mechanical energy balance method. *Acta Mechanica Solida Sinica* 24(2).

Rubio L, Munoz-Abella B and Loaiza G (2011) Static behavior of a shaft with an elliptical crack. *Mechanical Systems and Signal Processing* 25: 1674–1686.

Saeed RA, Galybin AN and Popov V (2012) Crack identification in curvilinear beam by using ANN and ANFIS based on natural frequency and frequency functions. *Neural Compute and Application* 21: 1629–1645.

Sayyad FB, Kumar B and Khan SA (2013) Approximate analytical method for damage detection in free–free beam by measurement of axial vibrations. *International Journal of Damage Mechanics* 22: 133–142.

Sen F, Pakdil M, Sayman O, et al. (2011) Experimental failure analysis of glass-epoxy laminated composite bolted-joints with clearance under preload. *International Journal of Damage Mechanics* 20(2): 163–178.

Shooshtari A and Khajavi R (2010) An efficient procedure to find shape functions and stiffness matrices of non prismatic Eulerer-Bernoulli and Timoshenko beam elements. *European Journal of Mechanics A/Solids* 29: 826–836.

Sugeno M and Kang GT (1988) Structure identification of fuzzy model. *Fuzzy Sets and System* 28: 15–33.

Suresh SS, Omkar N, Ganguli R, et al. (2004) Identification of crack location & depth in a cantilever beam using a modular neural network approach. *Smart Material & Structure* 13: 907–916.

Takagi T and Sugeno M (1985) Fuzzy identification of systems and its application to modeling and control. *IEEE Transaction on System, Man and Cybernetics* 15: 116–132.

Zachanias J, Hartman C and Delgado (2004) A damage detection on creates of beverages by artificial neural network & trained with finite element data. *Computer Methods Applied Mechanics and Engineering* 193: 561–574.

Zadeh LA (1995–1998) *Fuzzy Logic Toolbox User Guide*. Version 2. Berkeley, CA: The Math Works.

Zhu SP, Huang HZ and Wang ZL (2011) Fatigue life estimation considering damaging and strengthening of low amplitude loads under different load sequences using fuzzy sets approach. *International Journal of Damage Mechanics* 20(6): 876–899.

Appendix

Notation

a	width of the crack
amd	average relative first mode shape difference
A	cross-sectional area of the shaft
A_i ($i = 1$ to 18)	unknown coefficients of the matrix
bmd	average relative second mode shape difference
B_i ($i = 1, 2 \ldots$)	depth of the crack
cmd	average relative third mode shape difference
$C_{i,j}$ ($i = 1, 2, 3$)	stress intensity factor
$\overline{C}_v$	$\frac{\omega L}{C_v}$
$\overline{C}_y$	$\left(\frac{\omega L}{S_y}\right)^{1/2}$
D	diameter of the shaft
E	Young's modulus of elasticity of the shaft material
fnf	relative third natural frequency
$F_{i,j}$ ($i = 1, 2$)	axial force ($i = 1$), bending moment ($i = 2$)
h	coordinates of the crack surface
i	variable
inf	relative first natural frequency
j	variable
J_e	strain-energy release rate
L_i ($i = 1, 2 \ldots$)	location of the crack from one of the fixed end
mnf	relative second natural frequency
M_i ($i = 1 \ldots 8$)	compliance constant
$M_{i,j}$	$\frac{M_i}{M_j}$
P_i ($i = 1, 2$)	experimentally determined function
Q	system matrix
R_i ($i = 1, 2 \ldots 12$)	variable in Q matrix
$S_{i,j}$ ($i = 1, 2, 3$)	elements of the compliance matrix
$\overline{S}_v$	$\left(\frac{E}{\rho}\right)^{1/2}$
S_y	$\left(\frac{EI}{\mu}\right)^{1/2}$
T_i	period of vibration
v_i ($i = 1, 2, 3$)	normal function
w	height of the rectangular strip
x	coordinates of the shaft
Y	coordinates of the shaft
α	L_i/L, location of the crack of the shaft
β	b_i/D, depth of crack of the shaft
μ	$A\rho$
v	Poisson's ratio
ω	angular velocity of the shaft
	coordinate of the crack surface

ρ density of crack surface

$(')$ $\frac{\partial}{\partial x}$ dimension less variables

% Change in Natural Frequency(Ω_i) $\frac{f_i^{uncracked} - f_i^{cracked}}{f_i^{uncracked}} \times 100$ Where i defined as ith frequency of the system

% Change in vertical amplitude (η_i) $\frac{|\text{Max}(Y_{cracked} - Y_{uncracked})|}{\text{Max } Y_{cracked}} \times 100$

I   moment of inertia